SWSC

RESEARCH ARTICLE   OPEN ⧉ ACCESS

Overview of the 2015 St. Patrick's day storm and its consequences for RTK and PPP positioning in Norway

Knut Stanley Jacobsen* and Yngvild Linnea Andalsvik

Norwegian Mapping Authority, PO 600 Sentrum, 3507 Hønefoss, Norway
*e-mail: knut.stanley.jacobsen@kartverket.no

ABSTRACT

The 2015 St. Patrick's day storm was the first storm of solar cycle 24 to reach a level of "Severe" on the NOAA geomagnetic storm scale. The Norwegian Mapping Authority is operating a national real-time kinematic (RTK) positioning network and has in recent years developed software and services and deployed instrumentation to monitor space weather disturbances. Here, we report on our observations during this event. Strong GNSS (Global Navigation Satellite System) disturbances, measured by the rate-of-TEC index (ROTI), were observed at all latitudes in Norway on March 17th and early on March 18th. Late on the 18th, strong disturbances were only observed in northern parts of Norway. We study the ionospheric disturbances in relation to the auroral electrojet currents, showing that the most intense disturbances of GNSS signals occur on the poleward side of poleward-moving current regions. This indicates a possible connection to ionospheric polar cap plasma patches and/or particle precipitation caused by magnetic reconnection in the magnetosphere tail. We also study the impact of the disturbances on the network RTK and Precise Point Positioning (PPP) techniques. The vertical position errors increase rapidly with increasing ROTI for both techniques, but PPP is more precise than RTK at all disturbance levels.

Key words. Positioning system – Space weather – Storm – Ionosphere (auroral) – Irregularities

1. Introduction

On 17–18 March 2015, the first storm of solar cycle 24 to reach the G4 level on the NOAA scale (Poppe 2000) occurred. As March 17th is St. Patrick's day, we will refer to the storm as the St. Patrick's day storm. The storm was notable for two reasons: the first that it was at that point the strongest storm of the solar cycle, the second that space weather agencies around the world failed to predict it. Geomagnetic storm warnings had been issued, but only for a minor storm, which would not be a concern to most users. As an example, this is an extract of the weekly report by the space weather prediction centre of NOAA.[1]

Space weather outlook 16 March–11 April, 2015

Solar activity is expected to continue at moderate levels until 19 March when Region 2297 transits off the visible disk. ⋯⟨snip⟩⋯ Geomagnetic field activity is expected to be at unsettled to active levels with minor storm periods likely on 18 March due to a combination of CH HSS effects as well as the arrival of the 15 March CME by mid to late on 17 March.

The Norwegian Mapping Authority (NMA) is operating a national real-time kinematic (RTK) positioning network and has in recent years developed software and services and deployed instrumentation to monitor space weather disturbances. We have previously reported on the impact of a strong (G3 level) and a less-than-minor (below the G-scale) geomagnetic storm on our RTK service (Jacobsen & Schäfer 2012;

Andalsvik & Jacobsen 2014). Since then, we have deployed new instrumentation and further developed our analysis capability. In this paper we give an overview of the St. Patrick's day storm event as observed from Norway, and its impact on positioning using the network RTK and Precise Point Positioning (PPP) techniques.

Network real-time kinematic (RTK) positioning is a processing technique in which a single user receiver receives supporting data about several types of GNSS error sources from a network of receivers (Frodge et al. 1994; Rizos 2003). This allows the user receiver to eliminate a large part of the errors in the signal and thus achieve an accurate position solution in real-time. At the time of the event, the software used for the central network processing at NMA was RTKNet, from the company Trimble.

Precise Point Positioning (PPP) is a single receiver processing strategy for GNSS observations that enables the efficient computation of high-quality coordinates, utilizing undifferenced dual-frequency code and phase observations by using precise satellite orbit and clock data products. More detailed descriptions of PPP can be found in e.g. Zumberge et al. (1997) and Kouba & Héroux (2001).

Kamide & Kusano (2015) were the first to report on the St Patrick's day storm in a scientific journal, in the form of a news article in the Space Weather journal. In addition to a general overview and comments regarding the event, they suggested that it was caused by a superposition of two moderate events. Cherniak et al. (2015) studied the disturbances on a global scale using data from more than 2500 GPS receivers. Their paper provides an excellent overview of the large-scale distribution and development of GPS disturbances.

One of the possible causes of GPS disturbances at high latitudes are polar cap patches, which are convecting clouds of

---

[1] NOAA/SWPC, 2015, ftp://ftp.swpc.noaa.gov/pub/warehouse/2015/WeeklyPDF/prf2063.pdf

Table 1. List of GNSS equipment at sites.

Site name	Latitude	Longitude	GNSS receiver	RTK monitor	Scintillation receiver
Tromsø	69.540	18.940	TRO1	MTRM	TRO2
Vega	65.531	11.964	VEGS	–	VEG2
Steinkjer	63.859	11.502	–	MSTE	–
Hønefoss	59.980	10.249	HFS4	MHFS	–

enhanced plasma density (e.g. Weber et al. 1986; Krankowski et al. 2006; Kintner et al. 2007; Tiwari et al. 2010; Moen et al. 2012; Prikryl et al. 2013; Jin et al. 2014). They are either transported across the polar cap from the dense ionospheric plasma at the sunlit side of the Earth or created by particle precipitation in the cusp. To disturb GPS signals, patches must contain small-scale plasma structures, with scale sizes of decameters to kilometers (Hey et al. 1946; Basu et al. 1990, 1998; Kintner et al. 2007; Mushini et al. 2012). These are formed by plasma instability processes under suitable conditions. Comprehensive information on the topic of patches may be found in Carlson (2012). Several studies have shown that the distribution of scintillations at high latitudes is similar to the region of patch formation on the dayside and the region where patches enter the auroral oval on the nightside (Spogli et al. 2009; Prikryl et al. 2010; Jacobsen & Dähnn 2014; Jin et al. 2015). Patches have also been connected to the occurrence of substorms (Nishimura et al. 2013; Zou et al. 2014). In a recent multi-instrument case study by van der Meeren et al. (2015), the patches were only associated with scintillations when they were located in the region of auroral precipitation. They suggest that a combination of both patches and energetic particle precipitation may be required in order to produce strong scintillations in the auroral region, but that their work alone does not present enough evidence to make a firm conclusion regarding this.

The data sources are presented in Section 2. The observations are presented and discussed in Section 3. Finally, Section 4 provides a short summary of our conclusions.

2. Data sources

2.1. Solar wind – OMNIWeb

Solar wind data were downloaded from the OMNIWeb website (http://omniweb.gsfc.nasa.gov/) of the NASA Goddard Space Flight Center. The data are 1-min-averaged, spacecraft-interspersed, field/plasma data sets shifted to the Earth's Bow Shock nose. This data set is referred to as the High Resolution OMNI (HRO) data set, and a detailed explanation is located at http://omniweb.gsfc.nasa.gov/html/omni_min_data.html.

2.2. Equivalent ionospheric currents – IMAGE

Equivalent ionospheric currents were calculated by the Finnish Meteorological Institute (FMI), using magnetometer measurements from the IMAGE network (http://space.fmi.fi/image/). The currents were calculated using a 2D equivalent current model (Amm & Viljanen 1999).

2.3. Global Navigation Satellite System (GNSS) – Norwegian Mapping Authority (NMA)

Various GNSS data were collected by NMA's receiver networks. Table 1 lists the receivers that are explicitly used in this paper. Figure 1 shows the geographic location of the sites listed

in Table 1. These GNSS receivers are Trimble NETR8/NETR9 receivers. They contribute data to the network RTK service, and their measurements are also stored in the NMA's data archive. The data include GPS and GLONASS dual-frequency pseudo-range and carrier phase measurements at 1 Hz rate, and all data are used by the RTK service. The data from the archive have been used to calculate PPP coordinates using the GIPSY software, provided by NASA's Jet Propulsion Laboratory (JPL), in kinematic mode. Important models and parameters applied in the PPP solution are listed in Table 2. In addition, precise GPS orbit and clock products are provided from JPL. Note that GIPSY only used the GPS data, not the GLONASS data. Detailed information about GIPSY is located on the GIPSY website at https://gipsy-oasis.jpl.nasa.gov.

The RTK monitors are receivers set up to mimic users of our RTK service. They receive the RTK data stream in the same way as a normal user would and calculate their position every second. The RTK coordinate solutions from the monitors are stored in the data archive, but not the raw measurements.

The scintillation receivers are Septentrio PolaRxS receivers receiving dual-frequency GPS and GLONASS signals at a 100 Hz rate.

In this paper, we quantify position error by the standard deviation of the vertical coordinate over a 60-second interval. Thus, the position error seen in this paper reflects the noise level of the position solution, but not the long-term position stability. The reasons for this choice are:

– The effects of the ionospheric disturbances are dynamic. Their impact on the coordinate solution changes on short timescales. For scintillation effects, the impact on the receiver changes so fast and seemingly randomly that it is best viewed not as an offset or bias but as an increase of the noise.
– The magnitude of the short-term variation of the ionospheric disturbance in the coordinate is much higher than that of the long-term variation. Other error sources, such as multipath, have a greater impact on the long-term position stability than the ionospheric disturbances. In this paper, we investigate the effects of the ionospheric disturbances.

Data from the entire NMA GNSS receiver network, which covers the entire Norwegian territory with a maximum interstation distance of 70 km, are processed to calculate 2D maps of the state of the ionosphere every 5 min. The ROTI data used in this paper have been extracted from those maps.

2.3.1. ROTI, ROTI@Rec and ROTI@Ground

In several places throughout this paper, the terms "ROTI@Rec" and "ROTI@Ground" are used. They are measures of the general level of ionospheric disturbance that is affecting a receiver located on the ground (not air- or spaceborne). This section explains the definition of the terms, and how they relate to ROTI.
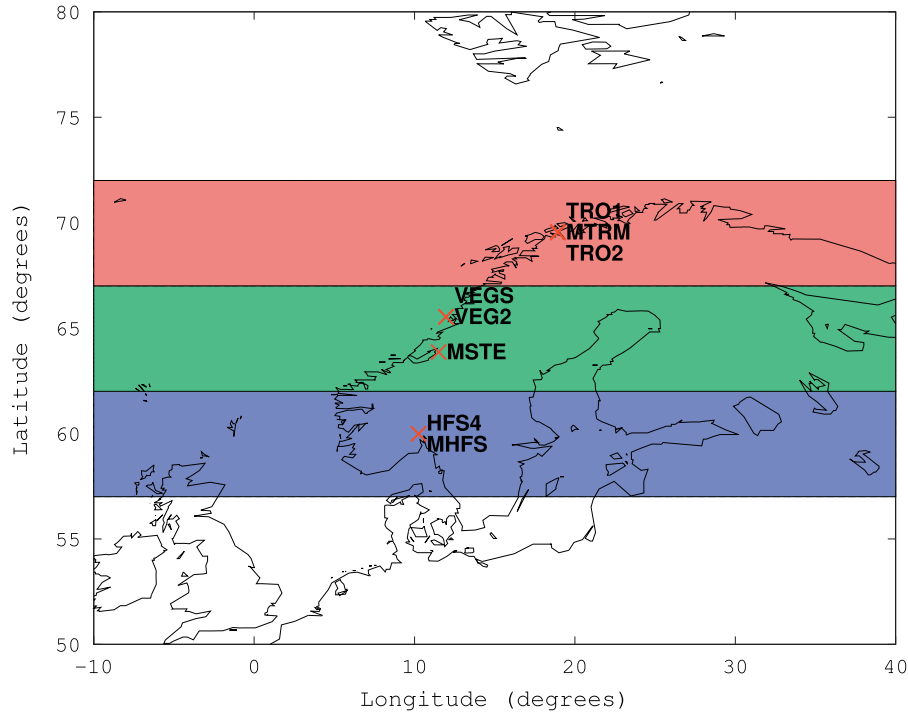
Fig. 1. The red crosses mark the locations of receivers that were used in time series and position error analysis in this paper. The coloured regions show the definition of three regions used in this paper. The blue area is the southern Norway region, the green is the middle Norway region and the red is the northern Norway region.

Table 2. Parameters/models used for the GIPSY PPP solution.

GIPSY version:	6.3
Reference frame:	IGb08
Elevation Angle Cutoff:	7°
Elevation dependent weighting:	Yes ($\sigma^2 = 1/\sqrt{\sin(\text{elevation})}$)
Antenna phase centre (receivers, transmitters):	Absolute based on IGS standard (igs08_1816.atx)
Troposphere mapping function:	VMF1
Tropospheric nominal values:	Wet and dry nominal values based on VMF1 grid model
2nd-order ionosphere model:	Based on IONEX files
Ocean loading:	FES2004
Ocean pole tide model	Yes
Ambiguity resolution:	Yes (Bertiger et al. 2010)

In the ionospheric monitor software, after data have been accumulated for 5 min, a ROTI value is calculated for each satellite seen by each receiver. (ROTI(*rec*, *sat*), where *rec* = receiver index, *sat* = satellite index) (For equations to calculate a ROTI value, see Jacobsen & Dähnn 2014.)

Each ROTI value can be associated with (1) the coordinate of the intersection of the receiver-to-satellite line with the thin-shell ionosphere (the ionospheric pierce point (IPP)) or with (2) the receiver. The height that we use for the thin-shell ionosphere model is 350 km.

When calculating the ionospheric ROTI, the ROTI values are assigned to the IPP coordinates. Then, the point cloud of ROTI values is interpolated to a regular 2D grid in longitude and latitude.

$$\text{ROTI}(\text{lon}, \text{lat}) = \text{InterpolationFunction}(\text{Set of all}[x_{\text{IPP}}(rec, sat),$$
$$\text{ROTI}(rec, sat)])$$
$$(1)$$

(x_{IPP} (*rec*, *sat*) is the coordinate of the IPP for receiver *rec* and satellite *sat*. ROTI(*rec*, *sat*) is the corresponding ROTI value.) The grids used for this paper have a spatial resolution

of 1×1 degrees. The ROTI data are interpolated using an inverse distance weighting function.

When calculating the ROTI@Ground, the average value of ROTI is calculated for each receiver

$$\text{ROTI@Rec}(x_{rec}) = \frac{1}{\text{NumSat}} \sum_{sat=\text{satellites}} \text{ROTI}(rec, sat) \quad (2)$$

(NumSat is the number of currently observed satellites, *satellites* is the set of satellites currently observed by the receiver and x_{rec} is the receiver coordinate for receiver *rec*.) The ROTI@Rec may be used directly or interpolated to a regular 2D grid in longitude and latitude.

$$\text{ROTI@Ground}(\text{lon}, \text{lat})$$
$$= \text{InterpolationFunction}(\text{Set of all}[x_{rec}, \text{ROTI@Rec}(x_{rec})])$$
$$(3)$$

To be explicit, Figure 2 displays ROTI@Ground, Figures 6–11 display ROTI@Rec, while Figures 3– 5 and 12 display ionospheric ROTI.
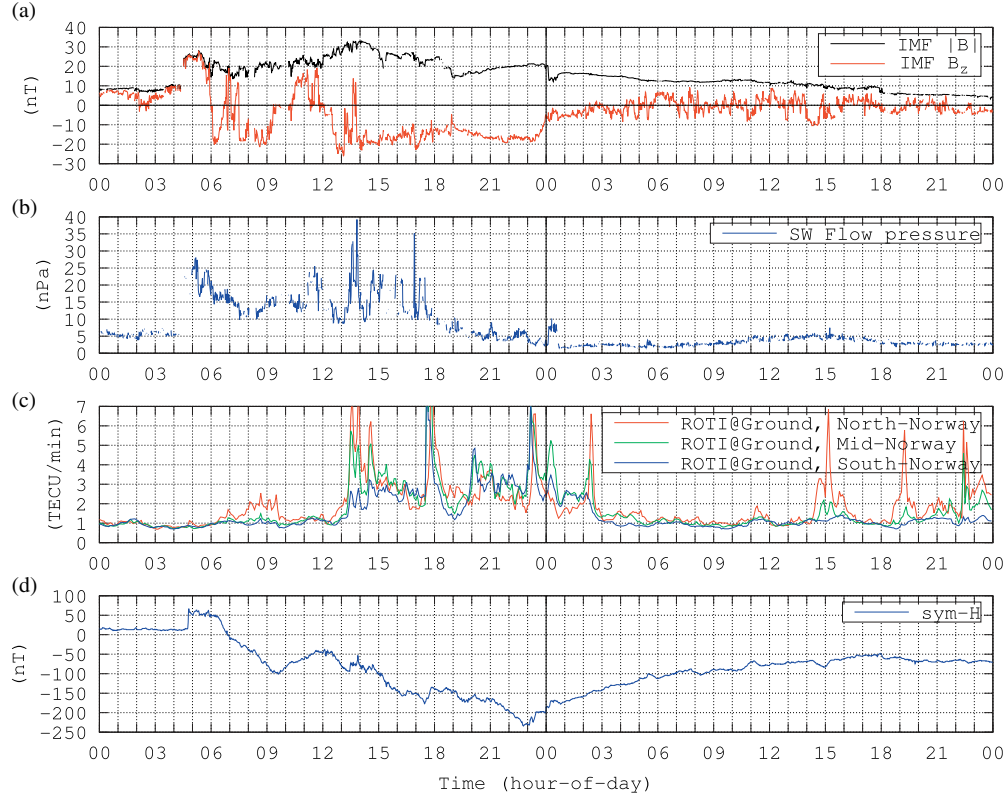
Fig. 2. Data for 2015-03-17 and 2015-03-18. (a): Solar wind magnetic field magnitude in black and Z-component (GSM) in red (timeshifted to the Bow Shock). (b) Solar wind flow pressure (timeshifted to the Bow Shock). (c) Average ROTI@Ground, for the three regions defined in Figure 1. (d) The SYM-H index.
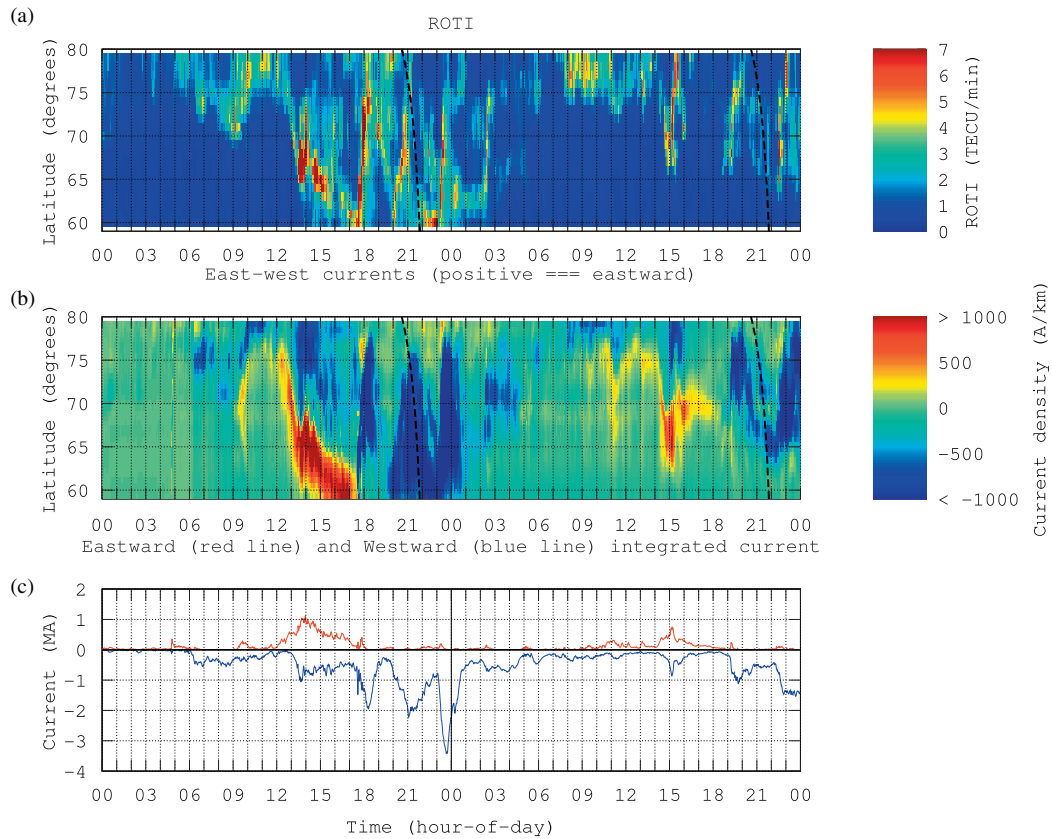

Fig. 3. Data for 2015-03-17 and 2015-03-18. (a) Average ROTI as a function of time and latitude, for the longitude range 20–24° East. (b) Equivalent ionospheric currents in the East-West direction as a function of time and latitude, at 22° East. (c) Total sum of eastward (red line) and westward (blue line) currents as a function of time. The dashed black line shows the location of MLT midnight.
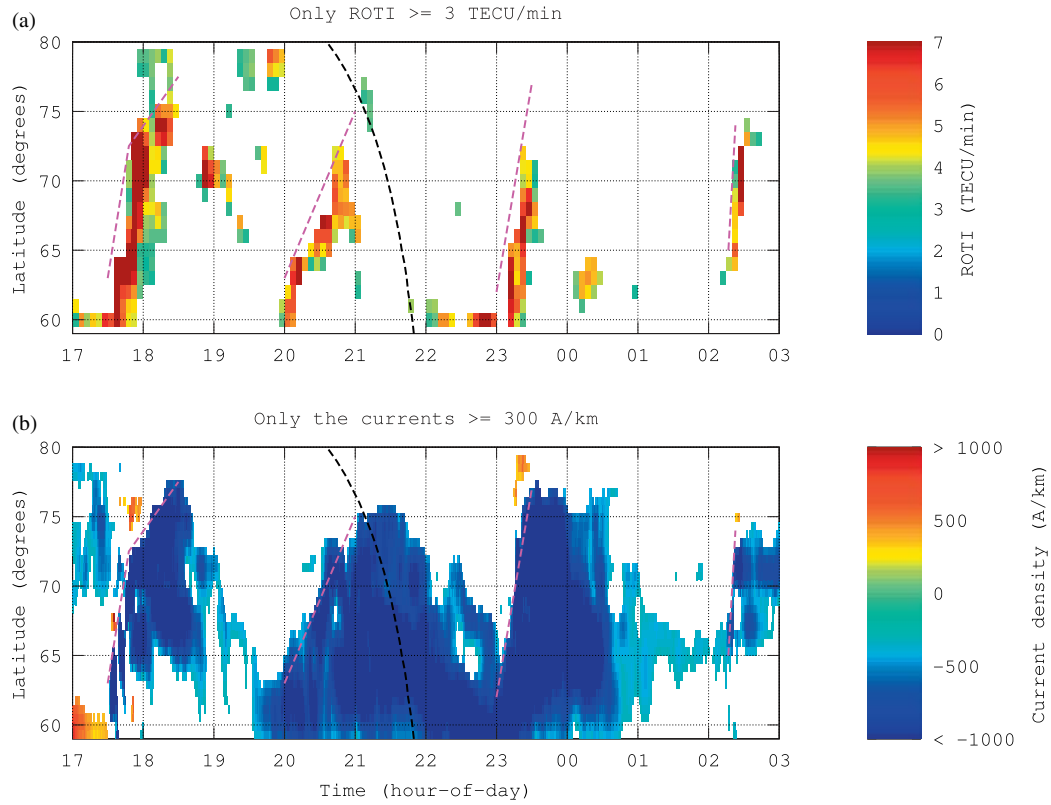
Fig. 4. This figure contains a subset of the data shown in the two panels (a) and (b) of Figure 3. (a) ROTI, filtered to show only strong disturbances. (b) East-West currents, filtered to show only strong currents. The dashed black line shows the location of MLT midnight. The dashed magenta lines are visual aids drawn on the poleward edge of the poleward-moving westward electrojet.
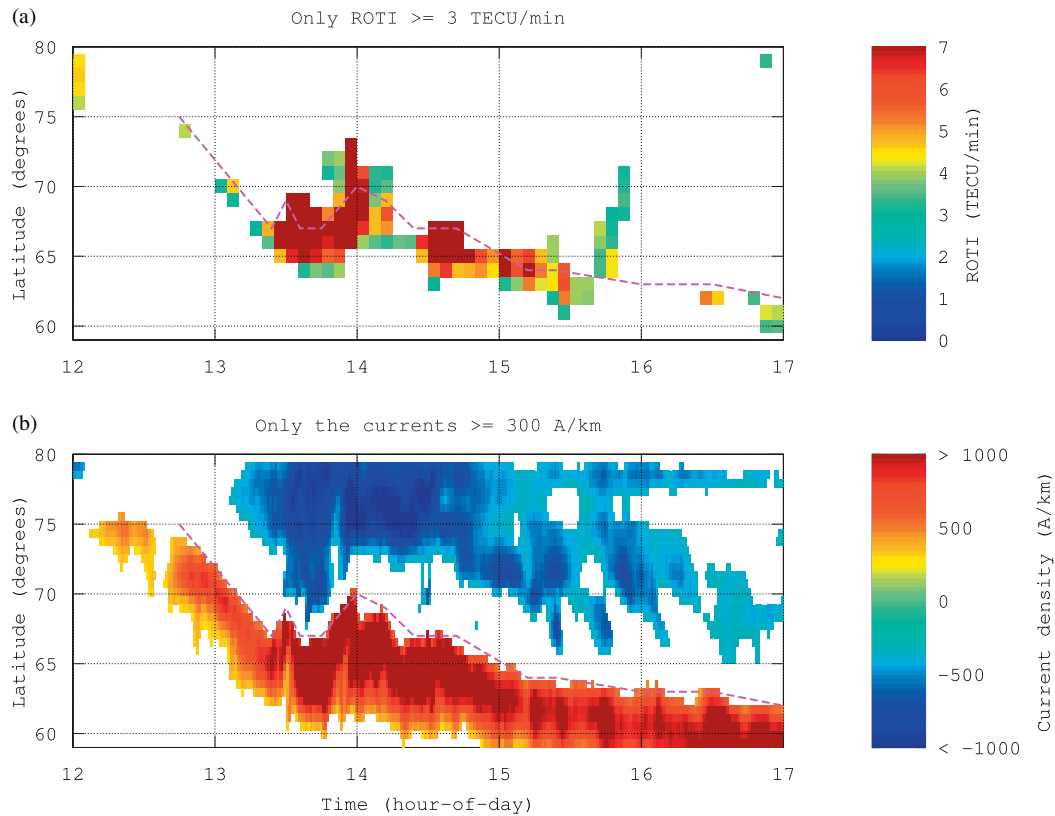

Fig. 5. This figure contains a subset of the data shown in the two panels (a) and (b) of Figure 3. (a) ROTI, filtered to show only strong disturbances. (b) East-West currents, filtered to show only strong currents. The dashed magenta line is a visual aid drawn on the poleward edge of the equatorward-moving eastward electrojet.
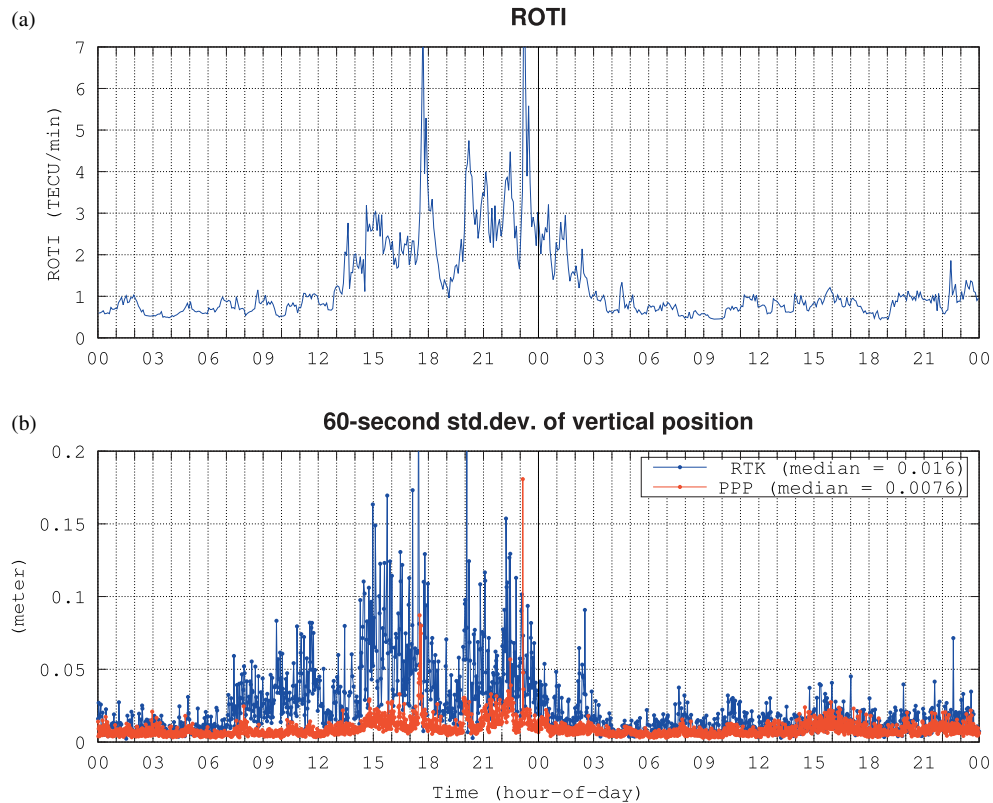
(a)

ROTI

(b)

60-second std.dev. of vertical position

Fig. 6. Data for 2015-03-17 and 2015-03-18. (a) ROTI@Rec for the receiver HFS4. (b) Position errors for Hønefoss (receivers MHFS & HFS4). Blue line is RTK, red line is PPP.

3. Observations and discussion

3.1. Solar wind and GNSS disturbance overview

Figure 2 shows solar wind magnetic field and pressure, ROTI@Ground for three regions and the SYM-H index. The CME impacted the Earth around 04:30 UT on the 17th, seen as a sudden increase of the magnetic field magnitude and solar wind pressure. The SYM-H index clearly shows a sudden commencement shortly thereafter. The geomagnetic storm increased in strength until 23:00 UT and spent the entire day of the 18th in recovery. At first, the Z-component of the interplanetary magnetic field (IMF) was strongly northward, which is not favourable for the solar wind – magnetosphere connection through reconnection at the dayside, and no GNSS disturbances were detected in Norway as seen from the ROTI in the panel (c).

At 06:00 UT there was a sudden change in IMF Bz, from +20 to −20 nT. Between 06:00 UT and 09:00 UT, it was mainly southward, but with some large northward excursions. Rising GNSS disturbance levels were seen in the north during this time, but the ROTI returned to the quiet level shortly after 09:30 UT, as the IMF Bz rose to 0.

Later, at 12:30 UT, the IMF Bz fell to −20 nT, and the GNSS disturbance levels started to rise. At 13:30 UT, GNSS disturbance levels rose very quickly, coinciding with magnetic field fluctuations and a rapid increase in pressure. Apart from a fluctuation around 14:00 UT, the IMF Bz continued to be strongly negative for most of this period until about 03:00 UT on the following day when it fluctuated around zero. The GNSS disturbance levels varied between moderate and strong from 12:30 UT on March 17 until 03:00 UT on the following day. Later on March 18, there were three short periods of
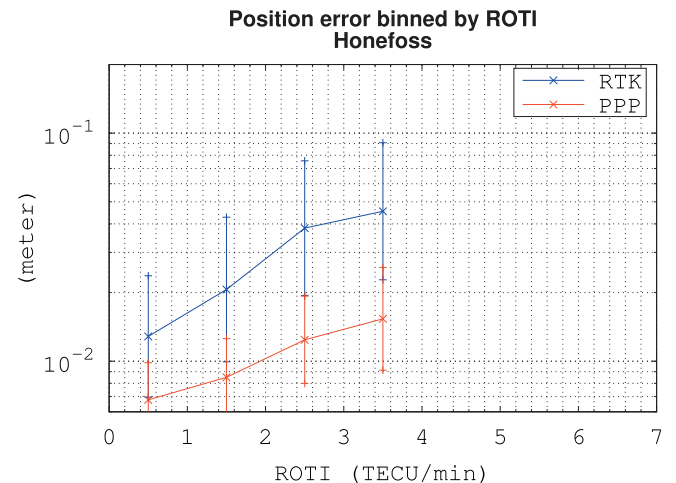
Position error binned by ROTI Honefoss

Fig. 7. Vertical position errors binned by ROTI@Rec, for Hønefoss (receivers MHFS & HFS4). The position error is defined as the standard deviation of the vertical coordinate over a 60-second interval. The blue line shows RTK error and the red line shows PPP error. Crosses mark the average value in each bin, while the the vertical lines show ± one standard deviation.

strong disturbances in the north that can be associated with intervals of moderately to weakly southward IMF Bz. Those were most likely due to substorms, releasing energy and particles that were left in the magnetosphere after the main event. Clear signs of geomagnetic activity can be seen in magnetograms (available online at http://space.fmi.fi/image), and in the calculated auroral currents which are presented in the next subsection.
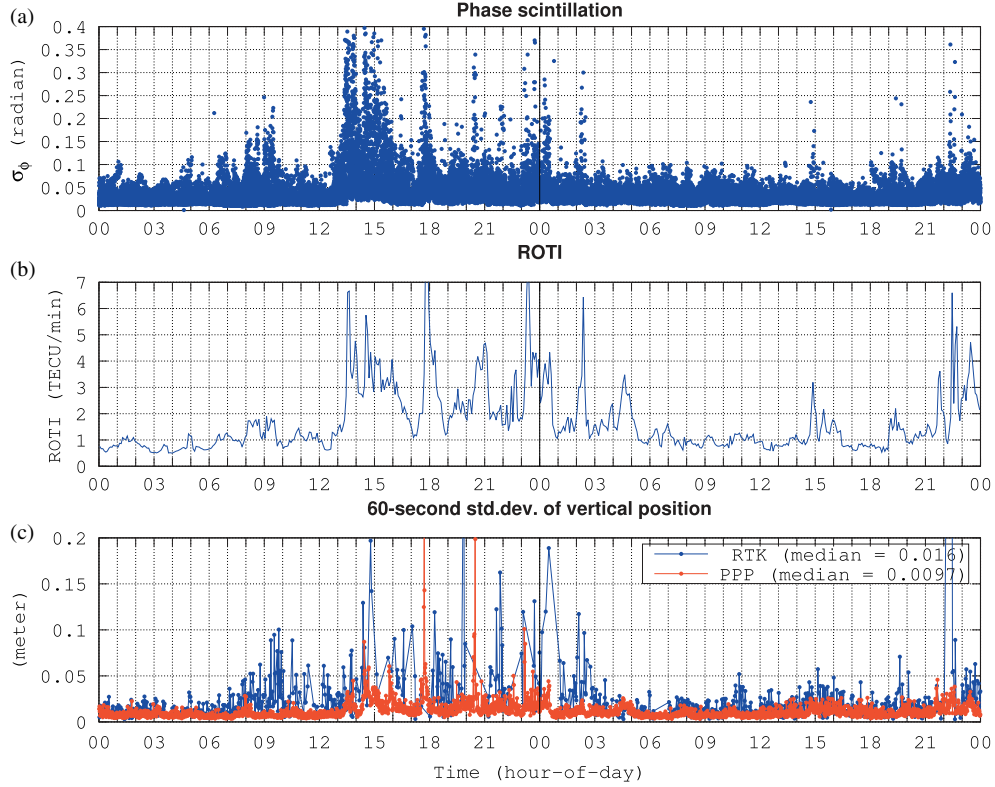
Fig. 8. Data for 2015-03-17 and 2015-03-18. (a) Phase scintillation index for all GPS and GLONASS satellites, from the scintillation receiver in Vega. (b) ROTI@Rec for the receiver VEGS. (c) Position errors for Steinkjer (RTK) and Vega (PPP) (receivers MSTE & VEGS). Blue line is RTK, red line is PPP.

3.2. Auroral electrojet

The panel (a) of Figure 3 shows ionospheric ROTI as a function of time and latitude. For each time and latitude, the value shown is the average value of ROTI in the longitude range of 20 to 24° East. Panel (b) shows the East-West component of the equivalent ionospheric currents at 22° East, calculated based on ground magnetometer measurements. The time and latitude axes are the same as for the panel (a). Panel (c) shows the total value (i.e. integrated over all latitudes) of the East-West currents. Strong ROTI values and strong currents were observed between 12:00 UT on the 17th and 01:00 UT on the 18th.

The two panels (a) and (b) of Figure 3 clearly indicate that there is at least a co-variation between equivalent ionospheric currents and ionospheric density irregularities. However, while the general pattern is similar, they also clearly demonstrate that there is not a simple linear relationship between current density and irregularity strength. To take a closer look at this, we made a plot focusing on the strong currents and disturbances before and around midnight.

Figure 4 shows a zoomed-in view of the two panels (a) and (b), for times from 17:00 UT on the 17th to 03:00 UT on the 18th. The colour scales are the same as in Figure 3 but low ROTI (<3 TECU/min) and currents (<300 A/km) values are not shown, in order to emphasize the high values. The figure reveals that the disturbed area was located at the poleward edge of poleward-moving areas of westward current. This is most clearly seen around 18:00 UT, 20:00 to 21:00 UT and around 23:30 UT. The poleward edge of the electrojet is located just equatorward of the open-closed magnetic field line boundary.
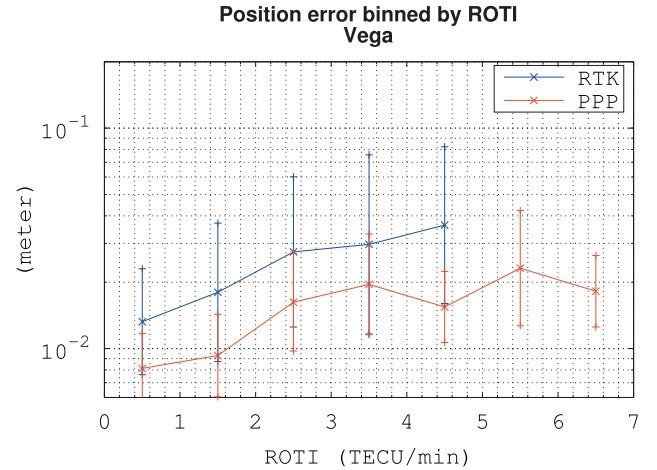

Fig. 9. Vertical position errors binned by ROTI@Rec, for Steinkjer (RTK) and Vega (PPP) (receivers MSTE & VEGS). The position error is defined as the standard deviation of the vertical coordinate over a 60-second interval. The blue line shows RTK error and the red line shows PPP error. Crosses mark the average value in each bin, while the the vertical lines show ± one standard deviation.

The location of the electrojet current moving poleward is a signature that tail reconnection dominates over dayside reconnection, while an equatorward motion indicates that reconnection at the dayside, where patches are produced, dominates (Cowley & Lockwood 1992; Lockwood & Cowley 1992; Milan et al. 2007). Equatorward motion may also occur without dayside reconnection in the recovery phase of as substorm (Akasofu 1964, 2013). There are two consequences of
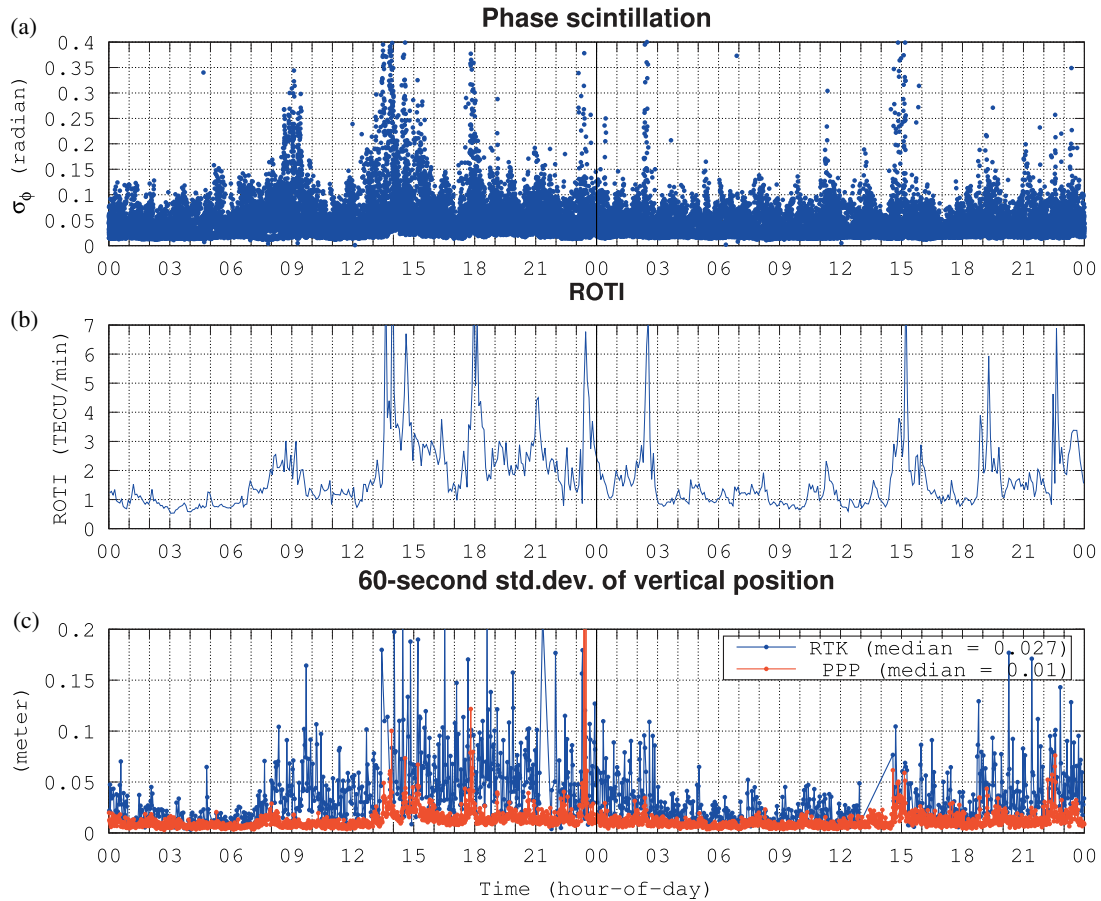
Fig. 10. Data for 2015-03-17 and 2015-03-18. (a) Phase scintillation index for all GPS and GLONASS satellites, from the scintillation receiver in Tromsø. (b) ROTI@Rec for the receiver TRO1. (c) Position errors for Tromsø (receivers MTRM & TRO1). Blue line is RTK, red line is PPP.

tail reconnection that could be linked to generation of iono-spheric irregularities that are observed as increased ROTI:

– when reconnection processes are ongoing in the tail, plasma patches will convect across the open-closed magnetic field boundary and then move on closed magnetic field lines towards the dayside;
– Energetic particle precipitation will occur in the auroral oval region. This may contribute to the structuring of existing patches.

Both of these phenomena would affect the region in which the ionospheric disturbances are observed. Unfortunately, the data available here cannot be used to distinguish between those effects. All-sky imaging data were poor or not available for this period due to cloud cover. Radar data were also not available for this region at this time. Thus, the work to determine the relative importance of those effects will have to be left to future events. We note that in the global view of this event in the paper by Cherniak et al. (2015), patches were observed to drift across the polar cap and enter the nightside auroral oval, and they were associated with significant increases in the intensity of ionospheric irregularities. In a case study of another event by Jin et al. (2014), patches that had entered the auroral region (auroral blobs) were directly connected to the strongest scintillations. In the case study by van der Meeren et al. (2015), scintillations were not observed for patches outside of the region of auroral emissions/particle precipitation, but strong scintilllation
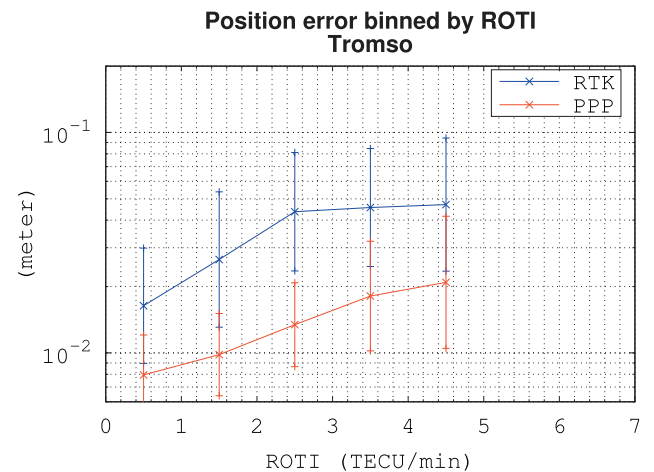

Fig. 11. Vertical position errors binned by ROTI@Rec, for Tromsø (receivers MTRM & TRO1). The position error is defined as the standard deviation of the vertical coordinate over a 60-second interval. The blue line shows RTK error and the red line shows PPP error. Crosses mark the average value in each bin, while the vertical lines show ± one standard deviation.

was observed in association with patches co-located with strong auroral emissions/particle precipitation. In-situ observations of patches by Moen et al. (2012) indicate that particle precipitation is a driver of plasma instabilities that form structures on scales that cause scintillation in GNSS signals.
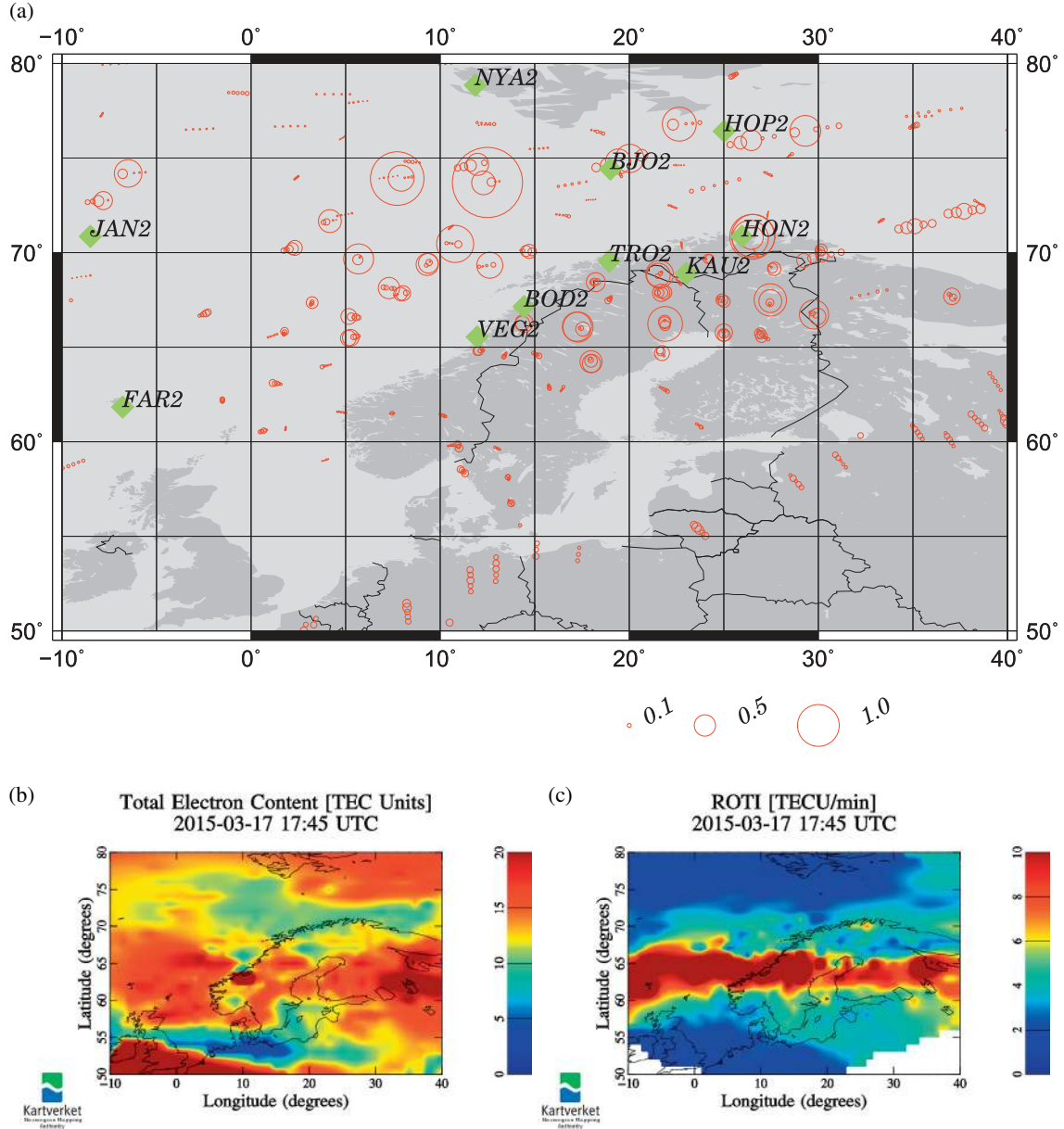
Fig. 12. Maps of phase scintillation, VTEC and ROTI for the time period 17:40–17:45 UT on March 17th. (a) Phase scintillation, (b) vertical TEC, (c) ROTI.

Figure 5 shows a zoomed-in view for 12:00 to 17:00 UT on the 17th, the time period that had a strong eastward current. Between 13:30 and 14:10 UT, the disturbed area is located between the region of eastward and westward currents, and the current regions as well as the disturbed region are alternating between poleward and equatorward motion. The combination of several concurrent effects makes the analysis of this time period complicated. Without other supporting non-GNSS measurements, the different phenomena cannot be conclusively identified and separated. From 14:30 to 15:30, the large ROTI values are located on the poleward edge of the equatorward-moving eastward current. However, this is not observed for the times 12:30 to 13:30 UT and 15:30 to 17:00 UT. We were not able to come to a conclusion regarding the physical mechanisms responsible for this behaviour, so we only make a note of this behaviour here and intend to return to this topic during investigations of future events.

3.3. Position errors

Figures 6, 8 and 10 show time series of phase scintillation (where available), ROTI and position errors for the southern, middle and northern Norway regions, respectively. In Figures 6 and 10, the receivers (GNSS, RTK monitor, scintillation) used are co-located, but for Figure 8 this was not possible. The RTK monitor receiver MSTE, which is used for the RTK coordinates, is approximately 180 km south of the other receivers shown in Figure 1 and approximately 14 km away from the closest RTK network receiver. This is still close enough for the time series comparisons to be valid, but it may suffer from additional errors due to its separation from the RTK network receivers, whereas the receivers at Hønefoss and Tromsø are co-located with a RTK network receiver.

To determine how the position errors vary with the ionospheric disturbances, they were sorted by the ROTI@Rec.

The bin size was 1 ROTI, and the values were not calculated for bins with less than 20 data points. In each bin, the mean value and the standard deviation were calculated. Figures 7, 9 and 11 show the results. In Figure 9 PPP have results for higher ROTI than RTK. This is because the RTK processing was unable to provide enough coordinates when ROTI was at its highest levels. The effect can also be seen in Figure 8 by close examination of the time series, where there are fewer data points (blue dots) in the panel (c) during periods of high activity.

Hønefoss, which is located at 60° North, is generally unaffected by activity in the auroral oval during weak to moderate events, as the auroral oval is too far north to affect it. This event, however, was strong enough to expand the auroral oval so far south that even Hønefoss was impacted by the full effects of the storm at night on the 17th. Figure 6 shows the time series of ROTI and position errors. A strong response is seen in both ROTI and position errors between 12 UT on the 17th and 3 UT on the 18th. An increased level of error is also seen in the RTK coordinates in the hours prior to 12 UT, without any corresponding signature in the ROTI or PPP error. The likely cause of this are increased plasma gradients which cause difficulties for the network RTK processing, but which do not contain strong structuring at small scales. This could be caused by patches that are not structured at small scales.

Vega and Steinkjer are sites in the middle of Norway. Moderate or stronger geomagnetic storms tend to expand the auroral oval enough to disturb these sites. Figure 8 shows the time series of ROTI and position errors. As for Hønefoss, disturbances are observed between 12 UT on the 17th and 3 UT on the 18th. There are some position errors observed for RTK at around 9 UT, coinciding with some observations of low level phase scintillation and slightly enhanced ROTI. The PPP position does not show a visible increase in error at that time. There are also some small signs of disturbances at the end of the 18th.

Tromsø, at 70° North, is located beneath the auroral oval at night during normal conditions and thus frequently experiences ionospheric disturbances. Figure 10 shows the time series of ROTI and position errors. Like the other sites, it experienced moderate to strong disturbances between 12 UT on the 17th and 3 UT on the 18th, and some disturbances around 9 UT. Scintillations were observed around 9 UT, and these were stronger than those observed in the middle of Norway at the same time. An enhanced level of ROTI was also observed at that time, rising gradually from 6 to 9 UT, peaking around 9 UT and then falling back down to the quiet level. Tromsø was the only one of the three sites to experience significant positioning errors late on the 18th.

All of the sites observed short-lived peaks of the ROTI, coinciding with peaks in phase scintillation activity. The timing of the peaks corresponds to the times of intensified electrojet currents and poleward motion, or in some cases motion whose direction was unclear, of the current region. This means that the most intense disturbances, whether measured by ROTI or phase scintillation, were caused by substorms that result from active tail reconnection. This can be seen in Figures 3 and 4 and was discussed in the previous section.

Figures 7, 9 and 11 show the relation between ROTI and positioning errors. All of them show the same pattern of positioning errors increasing rapidly with increasing ROTI. The curves for the RTK and PPP techniques appear to be approximately parallel, meaning that the PPP technique yields more precise coordinates than RTK regardless of the ionospheric disturbance level.

3.4. Scintillation example

Figure 12 shows phase scintillation measurements from NMA's scintillation receiver network, and simultaneous maps of VTEC and ROTI for the same geographical area. The scintillation receivers were located in Bjørnøya, Bodø, The Faroe Islands, Honningsvåg, Hopen, Jan Mayen, Kautokeino, Ny-Ålesund, Tromsø and Vega, and are plotted as green diamonds in panel (a). In panel (a), the GPS and GLONASS phase scintillation indices are plotted individually for each scintillation measurement. The size of the circles is proportional to the strength of the scintillation. To show the scale, below the plot three circles are drawn along with the corresponding scintillation values in radians. The plot contains data from 5 min of measurements. The scintillation index is calculated once per minute, so there are five data points for each satellite link. Scintillation measurements from satellites below 15° elevation are not plotted. Panels (b) and (c) show the total electron content and ionospheric ROTI maps, respectively. The VTEC map was produced by Kriging interpolation of the VTEC values at the IPPs. Information about the Kriging technique, and how it can be applied to ionospheric VTEC, can be found in e.g. Blanch (2004) and Sparks et al. (2011). The scales of the VTEC and ROTI maps have been adjusted to best show the anomalous conditions. For reference, a normal quiet-time level of ROTI is around 1 TECU/min, a normal peak daytime VTEC for southern Norway at this time of year is between 20 and 30 TECU, and a normal nighttime VTEC is around 5 TECU.

The strong phase scintillations are located in the area of enhanced (>3) ROTI, but they are not showing a preference for the area of very high (>7) ROTI. There is a lot of variation both spatially and temporally for the scintillation index. This may indicate that the scintillation is caused by smaller structures within the area of enhanced ROTI. Almost the entire area contains higher than normal values of VTEC, but the area in which there are very high ROTI values has particularly high VTEC values. The area of maximum VTEC value in the lower left corner of the plot is the edge of the region of sunlit plasma, and is not related to the space weather event. The amount of TEC is too high to have been produced locally, so transport of plasma from the dayside must have occurred. Within the region of very high VTEC values between 60 and 65° North there are most likely plasma patches. The resolution of the TEC map may not be sufficient to fully characterize the shape of individual patches, but the uneven distribution and high VTEC values seen in the plot are a strong indication that plasma patches are present in the area.

4. Conclusions

We have presented our observations of the 2015 St. Patrick's day geomagnetic storm. These are our main conclusions:

– strong GNSS disturbances were observed at all latitudes in Norway on March 17th and early on the 18th. Late on the 18th, strong disturbances were only observed in the northern parts of Norway;
– GNSS disturbances, measured by ROTI, were most intense on the poleward edge of poleward-moving electrojet currents. This is possibly related to patches and/or particle precipitation activity caused by active tail reconnection. The relative importance of these phenomena, or the importance of having both simultaneously, cannot be determined from our data;

– regions with less intense currents and/or eqatorward motion of the current region were associated with less severe GNSS disturbances;

– Positioning errors increased rapidly with ROTI for both the RTK and PPP techniques. PPP was most precise regardless of disturbance level.

References

Akasofu, S.-I. The development of the auroral substorm. *Planet. Space Sci.*, **12 (4)**, 273–282, 1964, DOI: 10.1016/0032-0633(64)90151-5.

Akasofu, S.-I. The relationship between the magnetosphere and magnetospheric/auroral substorms. *Ann. Geophys.*, **31 (3)**, 387–394, 2013, DOI: 10.5194/angeo-31-387-2013.

Amm, O., and A. Viljanen. Ionospheric disturbance magnetic field continuation from the ground to the ionosphere using spherical elementary current systems. *Earth, Planets and Space*, **51 (6)**, 431–440, 1999, DOI: 10.1186/BF03352247.

Andalsvik, Y.L., and K.S. Jacobsen. Observed high-latitude GNSS disturbances during a less-than-minor geomagnetic storm. *Radio Science*, **49 (12)**, 1277–1288, 2014, DOI: 10.1002/2014RS005418.

Basu, S., S. Basu, E. MacKenzie, W.R. Coley, J.R. Sharber, and W.R. Hoegy. Plasma structuring by the gradient drift instability at high latitudes and comparison with velocity shear driven processes. *J. Geophys. Res. [Space Phys.]*, **95 (A6)**, 7799–7818, 1990, DOI: 10.1029/JA095iA06p07799.

Basu, S., E.J. Weber, T.W. Bullett, M.J. Keskinen, E. MacKenzie, P. Doherty, R. Sheehan, H. Kuenzler, P. Ning, and J. Bongiolatti. Characteristics of plasma structuring in the cusp/cleft region at Svalbard. *Radio Science*, **33 (6)**, 1885–1899, 1998, DOI: 10.1029/98RS01597.

Bertiger, W., S.D. Desai, B. Haines, N. Harvey, A.W. Moore, S. Owen, and J.P. Weiss. Single receiver phase ambiguity resolution with GPS data. *J. Geod.*, **84 (5)**, 327–337, 2010, DOI: 10.1007/s00190-010-0371-9.

Blanch, J. Using kriging to bound satellite ranging errors due to the ionosphere, *Ph.D. thesis*, Stanford University, 2004.

Carlson, H.C. Sharpening our thinking about polar cap ionospheric patch morphology, research, and mitigation techniques. *Radio Science*, **47 (4)**, RS0L21, 2012, DOI: 10.1029/2011RS004946.

Cherniak, I., I. Zakharenkova, and R.J. Redmon. Dynamics of the high-latitude ionospheric irregularities during the 17 March 2015 St. Patrick's Day storm: ground-based GPS measurements. *Space Weather*, **13 (9)**, 585–597, 2015, DOI: 10.1002/2015SW001237.

Cowley, S., and M. Lockwood. Excitation and decay of solar-wind driven flows in the magnetosphere ionosphere system. *Ann. Geophys.*, **10**, 103–115, 1992.

Frodge, S.L., S.R. Deloach, B. Remondi, D. Lapucha, and R.A. Barker. Real-time on-the-fly kinematic GPS system results. *Navigation*, **41 (2)**, 175–186, 1994.

Hey, J.S., S.J. Parsons, and J.W. Phillips. Fluctuations in cosmic radiation at radio-frequencies. *Nature*, **158**, 234–234, 1946, DOI: 10.1038/158234a0.

Jacobsen, K.S., and M. Dähnn. Statistics of ionospheric disturbances and their correlation with GNSS positioning errors at high latitudes. *J. Space Weather Space Clim.*, **4**, A27, 2014, DOI: 10.1051/swsc/2014024.

Jacobsen, K.S., and S. Schäfer. Observed effects of a geomagnetic storm on an RTK positioning network at high latitudes. *J. Space Weather Space Clim.*, **2**, A13, 2012, DOI: 10.1051/swsc/2012013.

Jin, Y., J.I. Moen, and W.J. Miloch. GPS scintillation effects associated with polar cap patches and substorm auroral activity: direct comparison. *J. Space Weather Space Clim.*, **4**, A23, 2014, DOI: 10.1051/swsc/2014019.

Jin, Y., J.I. Moen, and W.J. Miloch. On the collocation of the cusp aurora and the GPS phase scintillation: a statistical study. *J. Geophys. Res. [Space Phys.]*, **120 (10)**, 9176–9191, 2015, DOI: 10.1002/2015JA021449.

Kamide, Y., and K. Kusano. No major solar flares but the largest geomagnetic storm in the present solar cycle. *Space Weather*, **13 (6)**, 365–367, 2015, DOI: 10.1002/2015SW001213.

Kintner, P.M., B.M. Ledvina, and E.R. de Paula. GPS and ionospheric scintillations. *Space Weather*, **5 (9)**, S09003, 2007, DOI: 10.1029/2006SW000260.

Kouba, J., and P. Héroux. Precise point positioning using IGS orbit and clock products. *GPS Solutions*, **5 (2)**, 12–28, 2001, DOI: 10.1007/PL00012883.

Krankowski, A., I. Shagimuratov, L. Baran, I. Ephishov, and N. Tepenitzyna. The occurrence of polar cap patches in TEC fluctuations detected using GPS measurements in southern hemisphere. *Adv. Space Res.*, **38 (11)**, 2601–2609, 2006, DOI: 10.1016/j.asr.2005.12.006.

Lockwood, M., and S.W.H. Cowley. Ionospheric convection and the substorm cycle. In: Substorms 1: Proceedings of the First International Conference on Substorms, Kiruna, Sweden, vol. **1**, European Space Agency, Nordvijk, The Netherlands, 99–109, 1992.

Milan, S.E., G. Provan, and B. Hubert. Magnetic flux transport in the Dungey cycle: a survey of dayside and nightside reconnection rates. *J. Geophys. Res. [Space Phys.]*, **112 (A1)**, A01209, 2007, DOI: 10.1029/2006JA011642.

Moen, J., K. Oksavik, T. Abe, M. Lester, Y. Saito, T.A. Bekkeng, and K.S. Jacobsen. First in-situ measurements of HF radar echoing targets. *Geophys. Res. Lett.*, **39 (7)**, L07104, 2012, DOI: 10.1029/2012GL051407.

Mushini, S., P. Jayachandran, R. Langley, J. MacDougall, and D. Pokhotelov. Improved amplitude and phase-scintillation indices derived from wavelet detrended high-latitude GPS data. *GPS Solutions*, **16 (3)**, 363–373, 2012, DOI: 10.1007/s10291-011-0238-4.

Nishimura, Y., L.R. Lyons, K. Shiokawa, V. Angelopoulos, E.F. Donovan, and S.B. Mende. Substorm onset and expansion phase intensification precursors seen in polar cap patches and arcs. *J. Geophys. Res. [Space Phys.]*, **118 (5)**, 2034–2042, 2013, DOI: 10.1002/jgra.50279.

Poppe, B.B. New scales help public, technicians understand space weather. *Eos Trans. AGU*, **81 (29)**, 322–328, 2000, DOI: 10.1029/00EO00247.

Prikryl, P., R. Ghoddousi-Fard, B.S.R. Kunduri, E.G. Thomas, A.J. Coster, P.T. Jayachandran, E. Spanswick, and D.W. Danskin. GPS phase scintillation and proxy index at high latitudes during a moderate geomagnetic storm. *Ann. Geophys.*, **31 (5)**, 805–816, 2013, DOI: 10.5194/angeo-31-805-2013.

Prikryl, P., P.T. Jayachandran, S.C. Mushini, D. Pokhotelov, J.W. MacDougall, E. Donovan, E. Spanswick, and J.-P. St.-Maurice. GPS TEC, scintillation and cycle slips observed at high latitudes during solar minimum. *Ann. Geophys.*, **28 (6)**, 1307–1316, 2010, DOI: 10.5194/angeo-28-1307-2010.

Rizos, C. Network RTK research and implementation – a geodetic perspective. *JGPS*, **1 (2)**, 144–150, 2003.

Sparks, L., J. Blanch, and N. Pandya. Estimating ionospheric delay using kriging: 1. Methodology. *Radio Science*, **46 (6)**, RS0D21, 2011, DOI: 10.1029/2011RS004667.

Spogli, L., L. Alfonsi, G. De Franceschi, V. Romano, M.H.O. Aquino, and A. Dodson. Climatology of GPS ionospheric

scintillations over high and mid-latitude European regions. *Ann. Geophys.*, **27 (9)**, 3429–3437, 2009, DOI: 10.5194/angeo-27-3429-2009.

Tiwari, R., F. Ghafoori, O. Al-Fanek, O. Haddad, and S. Skone. Investigation of high latitude ionospheric scintillations observed in the Canadian region, in: Proceedings of the 23rd International Technical Meeting of the Satellite Division of the Institute of Navigation (ION GNSS 2010), Portland, OR, 349–360, 2010.

van der Meeren, C., K. Oksavik, D.A. Lorentzen, M.T. Rietveld, and L.B.N. Clausen. Severe and localized GNSS scintillation at the poleward edge of the nightside auroral oval during intense substorm aurora. *J. Geophys. Res. [Space Phys.]*, **120**, 10607–10621, 2015, DOI: 10.1002/2015JA021819.

Weber, E.J., J.A. Klobuchar, J. Buchau, H.C. Carlson, R.C. Livingston, O. de la Beaujardiere, M. McCready, J.G. Moore, and G.J. Bishop. Polar cap F layer patches: Structure and dynamics. *J. Geophys. Res. [Space Phys.]*, **91 (A11)**, 12121–12129, 1986, DOI: 10.1029/JA091iA11p12121.

Zou, Y., Y. Nishimura, L.R. Lyons, E.F. Donovan, J.M. Ruohoniemi, N. Nishitani, and K.A. McWilliams. Statistical relationships between enhanced polar cap flows and PBIs. *J. Geophys. Res. [Space Phys.]*, **119 (1)**, 151–162, 2014, DOI: 10.1002/2013JA019269.

Zumberge, J.F., M.B. Heflin, D.C. Jefferson, M.M. Watkins, and F.H. Webb. Precise point positioning for the efficient and robust analysis of GPS data from large networks. *J. Geophys. Res. [Solid Earth]*, **102 (B3)**, 5005–5017, 1997, DOI: 10.1029/96JB03860.